magnetochemistry

MDPI

Article

Magnetic and Impedance Analysis of Fe_2O_3 Nanoparticles for Chemical Warfare Agent Sensing Applications

Jennifer R. Soliz [1], Smriti Ranjit [2], Joshua J. Phillips [2], Richard A. Rosenberg [3] and Adam J. Hauser [2,*]

[1] US Army DEVCOM Chemical Biological Center, 5183 Blackhawk Road, Aberdeen Proving Ground, Edgewood, MD 21010-5424, USA; jennifer.r.soliz.civ@mail.mil
[2] Department of Physics and Astronomy, University of Alabama, Tuscaloosa, AL 35487, USA
[3] Advanced Photon Source, Argonne National Laboratory, Argonne, IL 60439, USA; rosenberg@anl.gov
* Correspondence: ahauser@ua.edu

Abstract: A dire need for real-time detection of toxic chemical compounds exists in both civilian and military spheres. In this paper, we demonstrate that inexpensive, commercially available Fe_2O_3 nanoparticles are capable of selective sensing of chemical warfare agents (CWAs) using frequency-dependent impedance spectroscopy, with additional potential as an orthogonal magnetic sensor. X-ray magnetic circular dichroism analysis shows that Fe_2O_3 nanoparticles possess moderately lowered moment upon exposure to 2-chloroethyl ethyl sulfide (2-CEES) and diisopropyl methylphosphonate (DIMP) and significantly lowered moment upon exposure to dimethyl methylphosphonate (DMMP) and dimethyl chlorophosphate (DMCP). Associated X-ray absorption spectra confirm a redox reaction in the Fe_2O_3 nanoparticles due to CWA structural analog exposure, with differentiable energy-dependent features that suggest selective sensing is possible, given the correct method. Impedance spectroscopy performed on samples dosed with DMMP, DMCP, and tabun (GA, chemical warfare nerve agent) showed strong, differentiable, frequency-dependent responses. The frequency profiles provide unique "shift fingerprints" with which high specificity can be determined, even amongst similar analytes. The results suggest that frequency-dependent impedance fingerprinting using commercially available Fe_2O_3 nanoparticles as a sensor material is a feasible route to selective detection.

Keywords: chemical detection; impedance spectroscopy; chemical warfare agent structural analogs; iron oxide; X-ray magnetic circular dichroism

Citation: Soliz, J.R.; Ranjit, S.; Phillips, J.J.; Rosenberg, R.A.; Hauser, A.J. Magnetic and Impedance Analysis of Fe_2O_3 Nanoparticles for Chemical Warfare Agent Sensing Applications. *Magnetochemistry* **2023**, *9*, 206. https://doi.org/10.3390/magnetochemistry9090206

Academic Editor: Xuan Gao

Received: 18 July 2023
Revised: 13 August 2023
Accepted: 23 August 2023
Published: 25 August 2023

1. Introduction

Chemical warfare agents (CWA) are highly toxic chemical compounds that have lethal effects on humans and are dispersed as liquid, gas, or aerosol threats [1,2]. Real-time detection of toxic chemical compounds, more specifically CWA structural analogs, is a great need in both civilian (pesticide/herbicide buildup) and military (chemical weapons) spheres [3,4]. In civilian life, similar compounds are widely used in agriculture as herbicides/pesticides, despite environmental evidence that these chemicals have been transported through our water systems and into the food chain [5,6], with adverse health effects most keenly felt by our minor and prenatal subpopulations [7–12]. Efforts to detect and remove these chemicals continue, but current detection methods that are both sensitive and selective remain elusive [13–24].

The use of metal oxide nanoparticles in CWA detection and decontamination has been widely researched [1,25,26]. Metal oxyhydroxide nanoparticles are excellent candidates for the detection and removal of hazardous compounds owing to their large surface area-to-volume ratios and tailored surface functionality [27–31]. Metal oxyhydroxides include structures that are stable in various environmental conditions (temperature, humidity) but have strong, specific reaction mechanisms (hydrolysis, oxidation) with toxic compounds.

These properties suggest high chemical sensitivity and selectivity and, thus, are attractive for chemical sensing applications. Additionally, the dielectric properties and large surface areas of these materials are conducive to rapid responses toward real-time detection. Previous studies show the potential of metal oxide for developing electrochemical sensors, gas sensors, and biosensors to detect harmful gases and toxic pollutants [2,32–36]. A variety of metal oxides have been studied, including Al_2O_3 [37], TiO_2/WO_3 [38], CeO_2 [39,40], SnO_2 [41–43], Fe_2O_3 [35,44–46], and ZnO [47,48]. For instance, Štengl et al. studied the hydrolysis of CWA using TiO_2. They compared their result with the commercial product developed by NanoScale Corporation, FAST-ACT®, which is made up of TiO_2 and MgO for the decomposition of CWA, such as soman (GD), sulphur mustard, and VX agent [25,33].

Recently, metal oxide composites such as Fe_2O_3/graphene nanocomposite and transition metal doped metal oxide nanoparticles have shown promising results and received a great deal of attention due to their improvement in sensing performance and electrochemical properties [36,49–51]. Furthermore, due to their physiochemical properties, metal oxide nanoparticles are widely used in a range of applications. They are extensively used in (a) biomedical and bioengineering applications for tissue repair and regeneration [52], (b) the pharmaceutical industry for drug delivery and disease treatment [53], and (c) cosmetology and dermatology such as treatment creams, sunscreen, and deodorants [54].

In this work, we demonstrate that inexpensive, commercially available Fe_2O_3 nanoparticles may be of use in sensing and distinguishing between CWAs if we utilize frequency-dependent impedance spectroscopy (FDIS) to create frequency "fingerprints" for each analyte [55,56]. This technique takes advantage of changes in a dielectric sensor material due to adsorption or reaction of an airborne analyte upon contact. These changes can manifest as shifts in existing conduction frequencies or as new conduction pathways but with a common result of frequency-dependent shifts in the impedance spectra. This work shows that significant differences in the frequency dependence and direction of impedance shift can be found even between two very chemically similar analytes. From the perspective of sensor development, we demonstrate FDIS as a feasible route to improving selectivity without affecting the sensitivity or chemistry of the sensor dielectric. We perform element-specific X-ray absorption spectroscopy (XAS) and X-ray magnetic circular dichroism (XMCD) measurements to confirm reaction with tested analytes, characterize changes in the magnetic properties to determine the potential for orthogonal sensing, and show that the reactions are consistent with the previously reported redox (Fe_2O_3 to FeO) reaction [57–59].

2. Materials and Methods

Fe_2O_3 nanoparticles with a 30–60 m^2/g surface area were purchased from Nanostructured and Amorphous Materials, Inc., and were not altered or further purified. Our X-ray diffraction (XRD) results (Figure S1) confirmed two polymorphs of Fe_2O_3 are present, and α–Fe_2O_3 and γ–Fe_2O_3 adopt the R-3c and $P4_332$ space group symmetries, respectively. The refined lattice parameters and atomic positions are reported in Table S1, and our results are similar to Zhang et al. [30,60] and Sahoo et al. [42]. The occupancies and thermal isotropic positions were held constant within the refinement. Using the Scherrer Equation, a crystallite size of 23 nm was calculated for unexposed particles and 21 and 19 nm for particles after DMMP and DMCP exposures, respectively, evidence of chemical reactivity. The nanoparticles were exposed to 10 wt. % liquid dosage of four CWA structural analogs (DMMP, DMCP, DIMP, 2-CEES) and held within a sealed vial for 1 day. Nanoparticles were similarly exposed to (GA, G-type chemical warfare nerve agent) as above, for 1 h.

Element-specific X-ray absorption spectroscopy (XAS) and X-ray magnetic circular dichroism (XMCD) measurements of the Fe L and O K edges were taken at the soft (4-ID-C) X-ray beamline at the Advanced Photon Source at Argonne National Laboratory. The Fe L edge was collected in total electron yield mode, while the O K edge was taken in fluorescence mode to optimize signal strength. Both the applied magnetic field and incident X-rays were aligned 20° from the plane of the film surface. Sample powder was mounted on

conductive carbon tape to avoid possible charging, and an external magnetic field of 1T was used for XMCD measurements. Systematic errors introduced by (1) the placement of the absorption edge step and (2) the normalization of experimental spectra to the absorption edge step intensity are the dominant sources of error in our XMCD measurements. The case of (1) is further complicated as the Fe L edge requires a split edge step due to multiple oxidation values. As such, we have analyzed the data for the range of all reasonable step edge centroid energies, edge step splitting, and normalization values and report the average moment and error values consummate with the range of possible moments. The choice of placing the step edge at the white line maximum intensity will generally correspond with the lower magnitude moment values. Placing the step edge at the maximum derivative of the XAS (center of rising edge) with respect to energy will yield magnitude moment values in the upper end of the error range. Finally, normalization of the spectra to sit higher (lower) with respect to the intensity step will result in lower (higher) moment values.

Another route to sensor feasibility with Fe_2O_3 nanoparticles is that of frequency-dependent impedance spectroscopy (FDIS), in which even slight variations in analyte chemistry will change the chemical structure just enough to result in changes in the characteristic transport frequencies and/or the magnitude of the changed impedance. To test the feasibility of such an approach, nanoparticle powders were exposed as described previously, pressed into 25 mm diameter pellets for DMMP and DMCP and 13 mm diameter pellets for GA exposure, and then analyzed via impedance spectroscopy using a Solartron Analytical 1260 impedance analyzer equipped with a 1296 dielectric interface and 12962A sample holder with brass plates. AC impedance measurements were collected on bulk pellets over a frequency range of 10^{-2} to 10^{6} Hz with an applied voltage of 100 mV. The dwell time was 1 s with 5 points measured per frequency decade. Measurements were repeated three times, checked for consistency and drift, and then averaged.

3. Results

The hole number values used in this work result from estimates from X-ray photoelectron spectroscopy (XPS). Analysis of spectra taken on the DMCP-exposed sample yields a Fe^{3+}/Fe ratio in the sample of 0.26, an indicator of a reduction of Fe_2O_3 to FeO. All other samples were nearly identical and yielded a Fe^{3+}/Fe ratio of 0.65, reflective of mixed valency that is expected and previously seen in Fe_2O_3 nanoparticles [61,62]. This allows us to adjust the holes/Fe site value used in XMCD calculations for the DMCP exposed sample to 4.26 and find (based on oxygen loss) a 4.5% increase in Fe sites/g (and consequent 4.5% decrease in moment/Fe) for the purposes of our SQUID calculation and comparison.

The XAS and corresponding XMCD spectra at the Fe L edge are shown after exposure to each analyte (as well as the unexposed material for reference) in Figure 1. The most obvious difference exists in powder exposed to DMCP, which shows a much larger white line intensity. This increase is indicative of the significant Fe reduction seen in the XPS results and further evidence for a reduced hole/Fe site value. Applying the aforementioned hole estimates to the L edge sum rules, we arrive at the values and errors for the total, spin, and orbital moment values as written in Table 1 and displayed in graph form in Figure 2 [63].

For both the unexposed and analyte-exposed Fe_2O_3 samples, spin moment (m_s) is larger than the orbital moment (m_l). We found that the m_l/m_s ratio for the unexposed sample is larger compared to the exposed Fe_2O_3 samples to analytes, suggesting the reduction in the orbital moment. This decrease in orbital moment is observed for all four exposed samples, and in the case of DMCP, the reduction in orbital moment is very large, approximately 96%. The spectroscopic splitting factor, g-factor $g = 2\left(1 + \frac{m_l}{m_s}\right)$ is calculated using the orbital-moment-to-spin moment ratio [64]. The values are compared to the magnetic moment values per Fe site, as measured by SQUID magnetometry (Quantum Design Magnetic Property Measurement System (MPMS)) at the same temperature. Our hole estimates result in total moment values by XMCD analysis that fit well with our

magnetometry values. Note that the relative XA intensity for the Fe L_2 edge is plotted in Figure 3a.

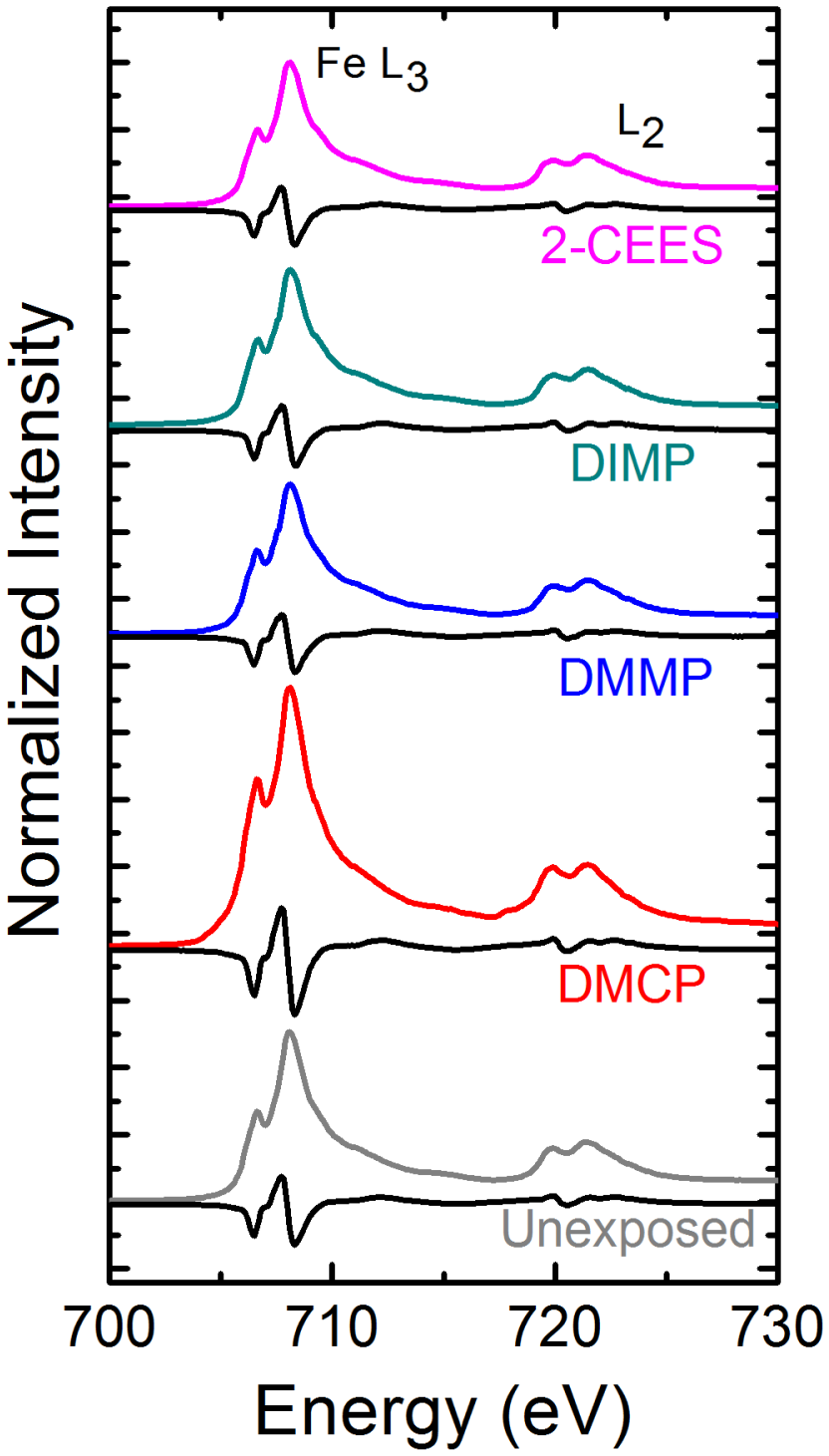

Figure 1. Normalized XANES and XMCD spectra at the Fe L edge for Fe_2O_3 nanoparticles exposed to various analytes, as well as unexposed material. XANES (XMCD) spectra are on top (bottom) within each pair, with analytes labeled below each pair.

Table 1. Magnetization results with an applied 1 T magnetic field by XMCD and comparison to SQUID Magnetometry results published previously on the powder samples.

Compound	Fe L_3/L_2 Branching Ratio	Spin Moment m_S per Fe by XMCD (μ_B/Fe)	Orbital Moment m_L per Fe by XMCD (μ_B/Fe)	m_L/m_S	g-Factor	Total Moment per Fe Site by XMCD (μ_B/Fe)	Magnetization per Fe Site by SQUID (μ_B/Fe)
Fe_2O_3	3.0 (2)	0.91 (4)	0.12 (2)	0.13 (2)	2.26 (2)	1.03 (5)	1.03
Fe_2O_3, DMCP	3.0 (1)	0.60 (3)	0.004 (4)	0.007 (6)	2.013 (6)	0.60 (3)	0.64
Fe_2O_3, DMMP	3.4 (2)	0.78 (4)	0.03 (1)	0.04 (1)	2.09 (1)	0.81 (4)	0.79
Fe_2O_3, DIMP	**3.3 (2)**	0.89 (4)	0.11 (2)	0.12 (2)	2.25 (2)	1.00 (5)	
Fe_2O_3, 2-CEES	**3.0 (2)**	0.84 (4)	0.09 (1)	0.10 (1)	2.21 (1)	0.92 (4)	

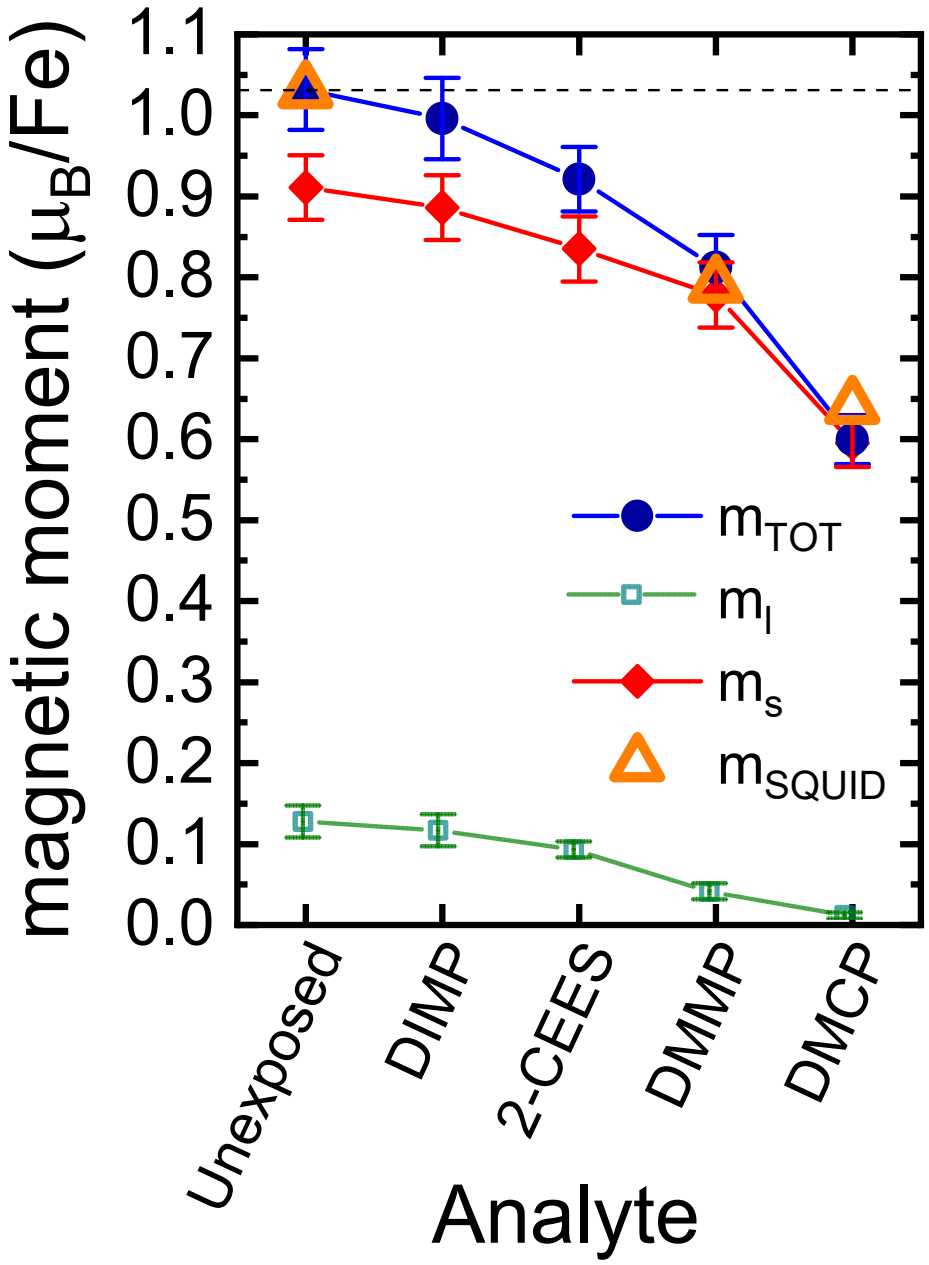

Figure 2. Spin (solid red diamond), orbital (open green square), and total (solid navy circle) magnetic moment for Fe_2O_3 nanoparticles as received ("unexposed") and after exposure to analytes as labeled, as determined by XMCD. Corroborating measurements of the total magnetic moment by SQUID magnetometry are overlaid as hollow orange triangles.

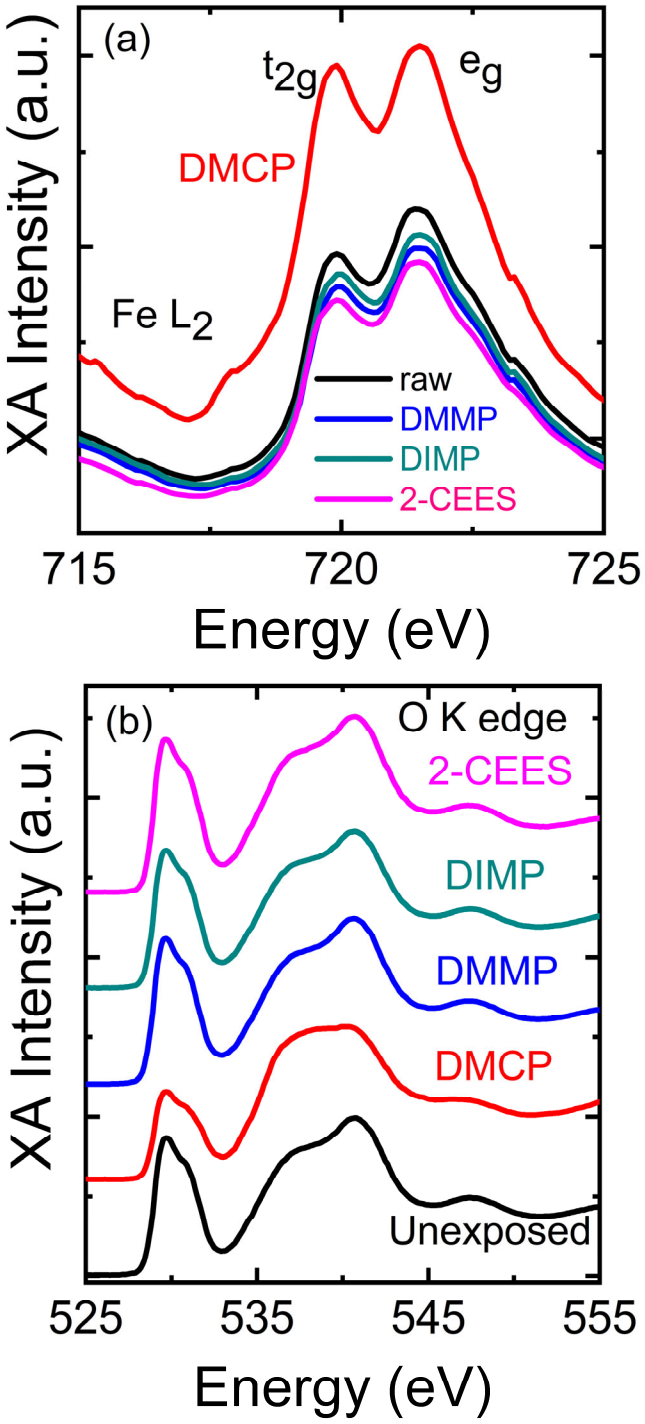

Figure 3. Normalized X-ray absorption spectra for different exposed samples at the (**a**) Fe L_2 and (**b**) O K edge.

As expected, the DMCP-exposed Fe_2O_3 nanoparticles show an approximately 40% decrease in magnetization as compared to unexposed material. The orbital moment drops to a statistically insignificant value, but a massive loss in the spin moment also occurs. This is likely the result of the reduction of Fe_2O_3 to FeO and a loss of orbital ordering as the unchanged magnetic regions become smaller and more isolated, inhibiting long-range ordering. Interestingly, different CWA structural analogs show different drop-offs in magnetization: DMMP-exposed samples show a smaller but still robust 20% decrease in total moment and a loss of nearly all orbital moment, while DIMP shows only a very slight

decrease that is well within the bounds of our estimated experimental uncertainty and can be considered statistically insignificant. Meanwhile, the same exposure dosage to 2-CEES results in a moderate (~10%) decrease in total and orbital moments that is statistically significant by our estimates.

The magnetic characterization results are consistent with the previously reported reaction pathway in Fe_2O_3 to organophosphate compounds [57,58]. We more directly observe the chemical changes in Figure 3a,b, which show normalized and overlaid XAS spectra for the Fe L_2 and O K edges, respectively. In addition to the larger white line intensity already discussed, the Fe L_2 spectra (resulting from the excitation of $2p_{1/2}$ orbitals to unoccupied *d* or *s* states) show a higher t_{2g}/e^*_g intensity ratio for DMCP exposure as compared to other exposures, which show little change compared to unexposed material. Generally speaking, the probability of absorption is proportional to the density of unoccupied states, so a relative increase in the t_{2g} orbital results from the reduction of Fe^{3+} to Fe^{2+}. Likewise, the O *K* edge shows similar results for all exposures except DMCP, in which the spectra (while still clearly in a mixed state) begin to more strongly resemble standards previously reported for FeO than that of Fe_2O_3 [65,66]. The O K edge XAS spectra reflect the electron transition from the O 1*s* core level to the O 2*p* unoccupied state and its hybridization with the orbitals of neighboring Fe ions.

The lower energy region between 528 and 534 eV indicates O 2*p* hybridization with Fe 3*d* states, while the higher energy region between 534 and 545 eV illustrates hybridization between O 2*p* and Fe 4*sp* orbitals [67]. The lower energy region of Fe_2O_3 spectra displays the two peak structure of Fe^{3+} high spin *d5* complex that can be attributed to t_{2g}-e_g split for octahedral sites or e-t_2 split for tetrahedral sites [67]. The intensity of analyte-exposed samples is close to the unexposed Fe_2O_3 sample, other than of the DMCP-exposed Fe_2O_3 sample, which decreases in the lower energy part of the spectra, and shows a change in positive to negative intensity at higher energy regions. These spectral changes are visible in Figure 4a,b which show the relative intensity and calculated difference spectra between X-ray absorption measured for unexposed and exposed Fe_2O_3 samples, respectively.

Our spectroscopic results show that Fe_2O_3 nanoparticles exhibit the expected chemical reaction and show magnetic sensitivity to CWA structural analogs. The changes in the magnetic moment to our dosages are significant, but the data has a scalar value that decreases with all our explored analytes. Although this makes magnetic sensing less useful as a stand-alone technique for differentiating CWAs, it does have promise as an orthogonal technique in a composite sensing system. While detection by synchrotron X-ray absorption or magnetometry techniques is unfeasible for field or rapid detection, small electronic devices incorporating Fe_2O_3 nanoparticles may be a viable sensing option.

Samples dosed with DMMP and DMCP, simulants for G-type nerve agents, were chosen as they are (1) the most reactive analytes, as evidenced by Figure 2, and (2) the most similar compounds chemically, providing a test of frequency fingerprinting as a selective method. Samples were also exposed to tabun (GA, G-type chemical warfare nerve agent), and impedance measurements were performed to understand the changes from GA exposure and to distinguish from simulants of nerve agents using the shift in impedance.

The impedance magnitude $|Z|$ and phase angle θ of unexposed (black), DMMP-exposed (blue), and DMCP-exposed (red) Fe_2O_3 pressed pellets as a function of frequency are plotted in log-scale in Figure 5a,b, respectively. A normalization approximation for pellet thickness variance (less than 5% sample-to-sample) was applied to $|Z|$ values. The small variation did not qualitatively change the results of measurements. Each sample shows typical capacitive behavior at higher frequencies and resistive behavior at low frequencies. This is corroborated by the phase angle data, which trends from nearly 0° (resistive) to nearly 90° (capacitive) as the frequency increases. The most striking result of this work lies in the opposite impedance responses to DMCP and DMMP exposures in Figure 5a: Despite the similar chemical structure of the two analytes, Fe_2O_3 nanoparticles exposed to DMMP exhibit significantly increased impedance across the entire frequency

range measured, while exposure to DMCP resulted in a strong decrease in impedance at all but the very highest frequencies.

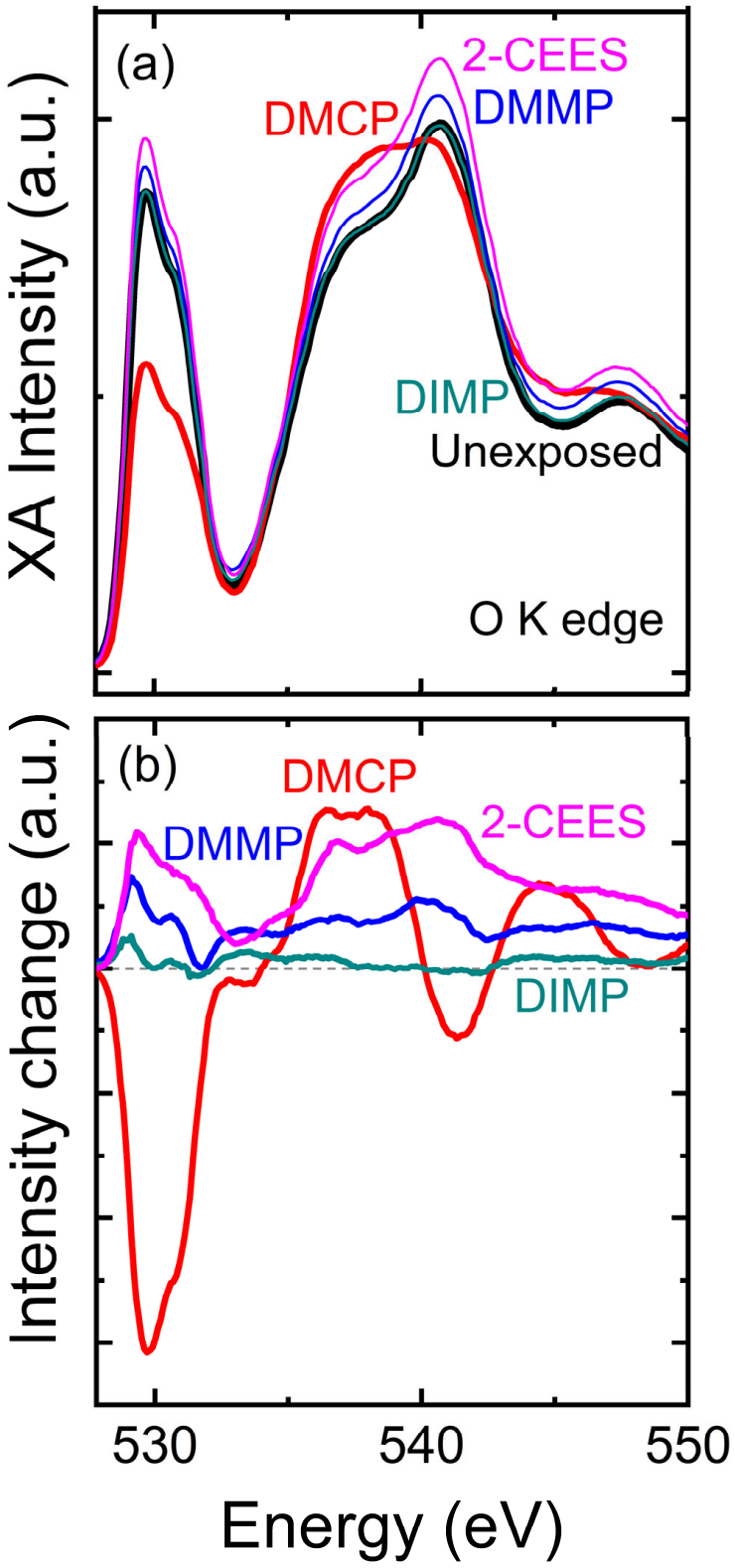

Figure 4. (**a**) O K-edge normalized XAS spectra of Fe_2O_3 samples, unexposed and exposed, and (**b**) Difference spectra of the exposed Fe_2O_3 samples, where the spectrum of the unexposed sample was subtracted from the different analyte-exposed samples.

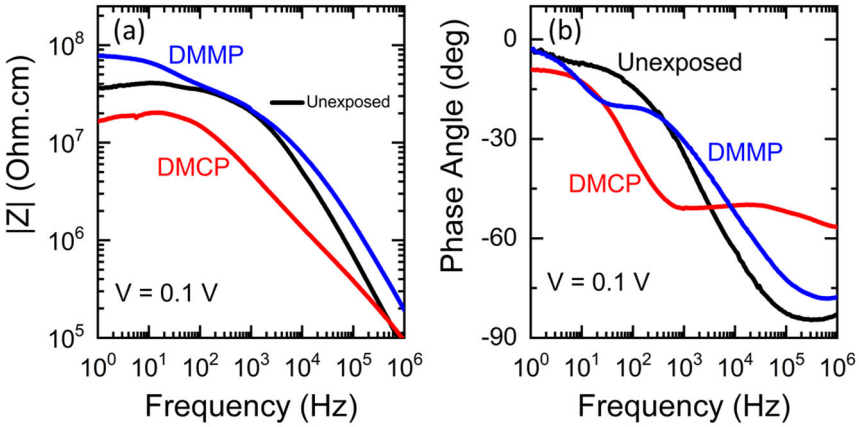

Figure 5. (**a**) Impedance magnitude |Z| and (**b**) phase angle as a function of the frequency of Fe_2O_3 nanoparticles before (black) and after exposure to DMCP (red) and DMMP (blue), as labeled.

Figure 6a,b shows the impedance magnitude and phase angle of unexposed (gray) and GA-exposed (green) Fe_2O_3 pressed pellets as a function of frequency. This sample shows a similar behavior as previous DMMP- and DMCP-exposed samples, suggesting a trend from capacitive to resistive when the frequency decreases from 1 MHz to 1 Hz, as shown in the phase angle plot. The impedance magnitude data in Figure 6a shows the decrease in magnitude at all frequencies measured, showing the bigger difference as frequency decreases from 1 MHz to 1 Hz.

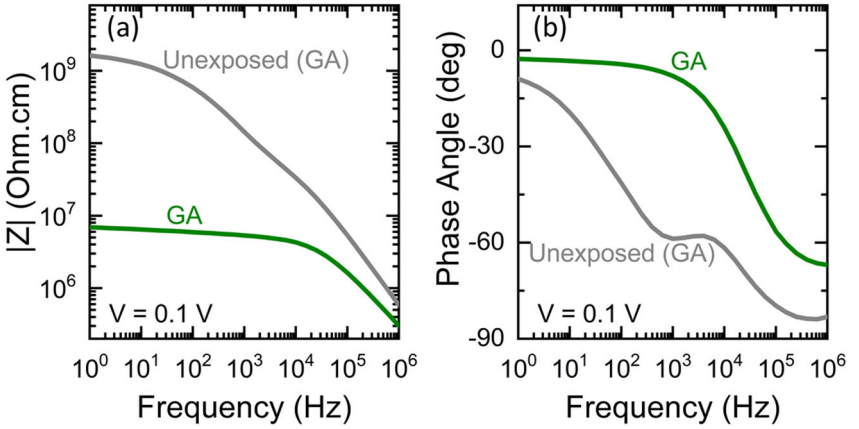

Figure 6. **(a**) Impedance magnitude |Z| and (**b**) phase angle as a function of the frequency of Fe_2O_3 nanoparticles before (gray) and after exposure to GA (green) as labeled.

Figure 7a replots the data in Figures 5a and 6a to show the percent change in the impedance magnitude due to DMMP, DMCP, and GA exposures. This plot accentuates the frequency-dependent features in Figure 5a: DMMP exposure creates large increases in |Z| at the low and high ends of the frequency regime and nearly no change from 10–100 Hz, while DMCP shows a crossover from negative to positive impedance change just below 1 MHz, an almost completely steady 50% decrease in |Z| from 1–100 Hz, and a maximum impedance drop of nearly 80% at approximately 2.5 kHz. Compared to DMMP and DMCP, GA exposure shows a decrease in impedance magnitude across the entire frequency range measured; there is a gradual decrease in |Z| from 1 MHz-1 kHz and then a steady decrease of 100% from 1 kHz–1 Hz. In Figure 7b, we extract the real component of the impedance (Z_{Re}) to derive a value for the electrical resistance $R = Z_{Re} = |Z| \cos(\theta)$, where θ is the phase angle measured and shown in Figures 5b and 6b. Below the kHz range, the system is dominated by resistive behavior, and so R and |Z| are closely related. At higher frequencies, we see large increases in resistance for both DMMP (460% @ 200 kHz) and DMCP (480% @ 550 kHz). The data in Figures 5b and 6b are replotted to show the

change in phase angle due to DMMP, DMCP, and GA exposure in Figure 7c. The change in phase angle shows strikingly different frequency-dependence when exposed to DMMP, DMCP, and GA exposures. The impedance magnitude and resistance drop by more than 99% upon GA exposure, while the phase shift is positive, that is, trending more capacitive. This seemingly incongruous group of results suggests sufficient decomposition to highly short any resistive region of the material left, increasing the overall weighting of capacitive regions (which are measured by the AC probe regardless of resistive shorting) compared to resistive regions (which are not fully probed when resistive shorts occur). We can observe initial signs of the resistive shorting in the negative phase shifts centered at 30 Hz in DMMP-exposed material and 300 Hz in DMCP-exposed material, leading to positive shifts (peaks centered at 100 kHz in DMCP-exposed material and 800 Hz in GA-exposed material, with a low, broad increase centered about 10 kHz for DMMP-exposed material) at the higher frequencies that more selectively probe capacitance. It is worth noting here both the size of the impedance increase as well as the large change in the frequency at which maximum phase shift occurs is useful in finding a combination of sensitivity and chemical differentiation/selectivity required for a potential sensing application.

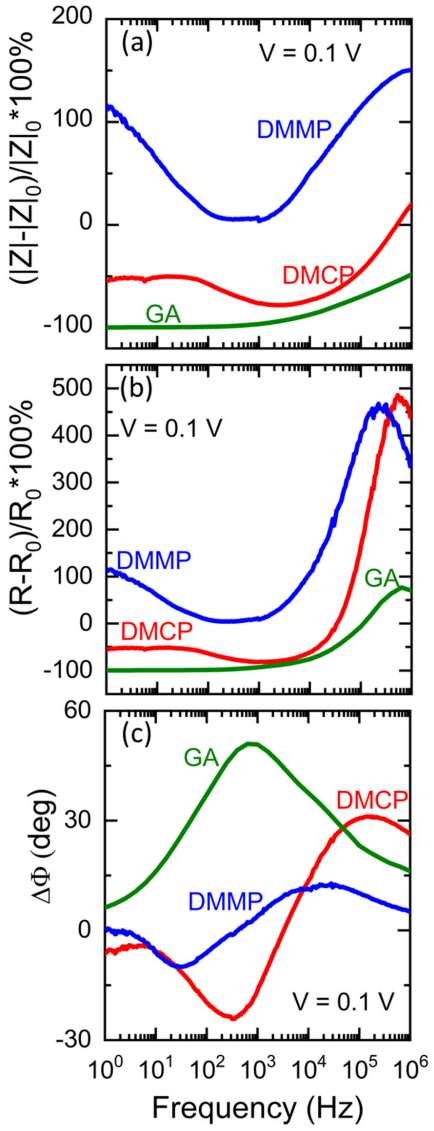

Figure 7. Percent changes in (**a**) impedance magnitude |Z| and (**b**) resistivity (R, the real component of the impedance), and (**c**) change in phase angle as a function of frequency for Fe_2O_3 nanoparticles after exposure to DMCP (red), DMMP (blue), and GA (green), as labeled above each curve.

4. Discussion

The sensitivity and selectivity of an impedance-based sensor are determined not only by the dielectric material being probed but also by the technique used and the method of analysis [68–71]. We note an array of other sensor methodologies to probe dielectrics, including pressure/strain-induced capacitive changes [72,73], optical detection [74–76], and chemiresistance/conductometrics [77–80]. The general challenge of choosing a dielectric material for airborne sensing lies in the trade-off between sensitivity and selectivity: If a material is sensitive to one analyte, it is often sensitive to many analytes, reducing its selectivity considerably. Modulation of chemistry has made strides in increasing selectivity, but the selectivity often comes at the price of sensitivity losses. Put glibly: *If a material is sensitive, it is sensitive to everything. If it is selective, it is not very sensitive to anything.*

Device technologies have advanced through this limitation via the use and cross-reference of many dielectric materials at once, creating something akin to an artificial nose with many types of point receptors to reasonable success. However, currently produced devices primarily use direct current or single-frequency AC modulation [78]. The results herein (combined with previous results [55,56,81,82]) suggest another potential route: Probing the same dielectric at a series of frequencies to create a frequency-dependent "fingerprint" of the system, reducing the need for as many elements or allowing a sensor the luxury of redundancy without increasing size, weight, power, and cost (SWaP-C) requirements. The FDIS technique can be employed to improve the selectivity of a device without adversely affecting the sensitivity of the sensor material's dielectric properties to the analyte of choice.

In this paper's case of Fe_2O_3, the stability born of a stable metal-oxide material combined with a specific (hydrolysis) reaction pathway does not, on its own, create sufficient selectivity for an organophosphate sensor: Just within this paper, we see a reaction from all organophosphates tested, as well as the non-organophosphate analog 2-CEES. Even limiting our FDIS scope to DMMP, DMCP, and GA, it would be very hard to identify (using the data in Figure 7) which analyte was present but for a few specific frequencies, and even in such a case, single-frequency detection of a combination of analytes is impossible. However, this changes considerably if one can use a range of frequencies—the shapes of the curves, in addition to the magnitudes, would help analysis considerably. It is important to note that a multi-analyte environment would almost certainly not yield a simple linear superposition of the single-analyte FDIS curves we show in this paper. However, it is nearly certain that the FDIS measurement approach would be of tremendous use in boosting the selectivity of any impedance-based sensor as described above.

5. Conclusions

XAS and XMCD results have provided evidence for varying levels of the expected $Fe_2O_3 \rightarrow FeO$ reaction due to contact with four CWA structural analogs. We find a range of significant decreases in the magnetic moment due to exposure to the analytes. The impedance results show that Fe_2O_3 nanoparticles have promise in the detection and differentiation of simulants DMMP and DMCP and between simulant and GA exposure if a device can be made to examine the frequency profile of the impedance and/or resistance. While the parallel-plate geometry utilized here with a pressed pellet is not conducive to sensitive airborne chemical detection, devices incorporating an electrically contiguous film or a porous structure with a high surface area could result in a detection device with excellent sensitivity and selectivity.

Supplementary Materials: The following supporting information can be downloaded at: https://www.mdpi.com/article/10.3390/magnetochemistry9090206/s1, Figure S1: X-ray powder diffraction pattern of Fe2O3 nanoparticles in 2θ range of 20 to 80 degrees. The black filled circles, red line, gray line, blue crosses, and pink crosses are the observed pattern, calculated pattern, difference curve between the observed and calculated curves, allowed Miller indices for space group P4332, and al-

lowed Miller indices for space group R-3c, respectively; Table S1: Lattice parameters, atomic positions, weight fractions, crystallite size, and RF2 factor from X-ray powder diffraction Rietveld refinement.

Author Contributions: Conceptualization, J.R.S., S.R. and A.J.H.; methodology, J.R.S., R.A.R., S.R. and A.J.H.; validation, A.J.H.; formal analysis, J.J.P., S.R. and A.J.H.; investigation, J.J.P., S.R. and R.A.R.; data curation, S.R. and A.J.H.; writing—original draft preparation, J.R.S. and S.R.; writing—review and editing, A.J.H.; supervision, J.R.S. and A.J.H.; J.R.S. and A.J.H. All authors have read and agreed to the published version of the manuscript.

Funding: Use of the Advanced Photon Source was supported by the U.S. Department of Energy, Office of Science, Office of Basic Energy Sciences, under Contract No. DE-AC02-06CH11357. A.J.H. acknowledges funding under U.S. Army Research Office STIR award #W911F-15-1-0104. This research was performed while J.R.S. held a National Research Council Research Associate Award at the U.S. Army DEVCOM Chemical Biological Center and was under the mentorship of Dr. Christopher Karwacki. The authors would also like to gratefully acknowledge the Defense Threat Reduction Agency for funding this work under CB10599.

Data Availability Statement: Data will be made available upon request.

Conflicts of Interest: The authors declare no conflict of interest. The funders had no role in the design of the study; in the collection, analyses, or interpretation of data; in the writing of the manuscript; or in the decision to publish the results.

References

1. Ganesan, K.; Raza, S.; Vijayaraghavan, R. Chemical warfare agents. *J. Pharm. Bioallied Sci.* **2010**, *2*, 166. [CrossRef]
2. Mukhopadhyay, S.; Schoenitz, M.; Dreizin, E.L. Vapor-phase decomposition of dimethyl methylphosphonate (DMMP), a sarin surrogate, in presence of metal oxides. *Def. Technol.* **2021**, *17*, 1095–1114. [CrossRef]
3. Munro, N. Toxicity of the Organophosphate Chemical Warfare Agents GA, GB, and VX: Implications for Public Protection. *Environ. Health Perspect.* **1994**, *102*, 18–37. [CrossRef]
4. Singh, B.; Prasad, G.; Pandey, K.; Danikhel, R.; Vijayaraghavan, R. Decontamination of Chemical Warfare Agents. *Def. Sci. J.* **2010**, *60*, 428–441. [CrossRef]
5. Curl, C.L.; Beresford, S.A.; Fenske, R.A.; Fitzpatrick, A.L.; Lu, C.; Nettleton, J.A.; Kaufman, J.D. Estimating pesticide exposure from dietary intake and organic food choices: The Multi-Ethnic Study of Atherosclerosis (MESA). *Env. Health Perspect* **2015**, *123*, 475–483. [CrossRef]
6. Rosenstock, L.; Keifer, M.; Daniell, W.E.; McConnell, R.; Claypoole, K. Chronic central nervous system effects of acute organophosphate pesticide intoxication. *Lancet* **1991**, *338*, 223–227. [CrossRef]
7. Engel, S.M.; Wetmur, J.; Chen, J.; Zhu, C.; Barr, D.B.; Canfield, R.L.; Wolff, M.S. Prenatal exposure to organophosphates, paraoxonase 1, and cognitive development in childhood. *Env. Health Perspect* **2011**, *119*, 1182–1188. [CrossRef]
8. Bouchard, M.F.; Chevrier, J.; Harley, K.G.; Kogut, K.; Vedar, M.; Calderon, N.; Trujillo, C.; Johnson, C.; Bradman, A.; Boyd Barr, D. Prenatal exposure to organophosphate pesticides and IQ in 7-year old children. *Environ. Health Perspect.* **2011**, *119*, 1189–1195. [CrossRef]
9. Singh, S.; Kumar, V.; Singh, P.; Banerjee, B.D.; Rautela, R.S.; Grover, S.S.; Rawat, D.S.; Pasha, S.T.; Jain, S.K.; Rai, A. Influence of CYP2C9, GSTM1, GSTT1 and NAT2 genetic polymorphisms on DNA damage in workers occupationally exposed to organophosphate pesticides. *Mutat. Res./Genet. Toxicol. Environ. Mutagen.* **2012**, *741*, 101–108. [CrossRef]
10. Lu, C.; Barr, D.B.; Pearson, M.A.; Waller, L.A. Dietary intake and its contribution to longitudinal organophosphorus pesticide exposure in urban/suburban children. *Env. Health Perspect* **2008**, *116*, 537–542. [CrossRef]
11. Eskenazi, B.; Bradman, A.; Castorina, R. Exposures of children to organophosphate pesticides and their potential adverse health effects. *Environ. Health Perspect.* **1999**, *107*, 409–419. [CrossRef] [PubMed]
12. Barr, D.B.; Wong, L.-Y.; Bravo, R.; Weerasekera, G.; Odetokun, M.; Restrepo, P.; Kim, D.-G.; Fernandez, C.; Perez, J.; Gallegos, M. Urinary concentrations of dialkylphosphate metabolites of organophosphorus pesticides: National Health and Nutrition Examination Survey 1999–2004. *Int. J. Environ. Res. Public Health* **2011**, *8*, 3063–3098. [CrossRef] [PubMed]
13. Kaur, N.; Thakur, H.; Pathak, S.; Prabhakar, N. Acetylcholinesterase immobilised eggshell membrane-based optical biosensor for organophosphate detection. *Int. J. Environ. Anal. Chem.* **2015**, *95*, 1134–1147. [CrossRef]
14. Janoš, P.; Kuráň, P.; Pilařová, V.; Trögl, J.; Šťastný, M.; Pelant, O.; Henych, J.; Bakardjieva, S.; Životský, O.; Kormunda, M. Magnetically separable reactive sorbent based on the CeO_2/γ-Fe_2O_3 composite and its utilization for rapid degradation of the organophosphate pesticide parathion methyl and certain nerve agents. *Chem. Eng. J.* **2015**, *262*, 747–755. [CrossRef]
15. Zenerino, A.; Boutard, T.; Bignon, C.; Amigoni, S.; Josse, D.; Devers, T.; Guittard, F. New CeO_2 nanoparticles-based topical formulations for the skin protection against organophosphates. *Toxicol. Rep.* **2015**, *2*, 1007–1013. [CrossRef]
16. Abdallah, M.A.-E.; Covaci, A. Organophosphate Flame Retardants in Indoor Dust from Egypt: Implications for Human Exposure. *Environ. Sci. Technol.* **2014**, *48*, 4782–4789. [CrossRef]

17. Baker, P.A.; Goltz, M.N.; Schrand, A.M.; Kim, D.-S. Organophosphate vapor detection on gold electrodes using peptide nanotubes. *Biosens. Bioelectron.* **2014**, *61*, 119–123. [CrossRef]
18. Janos, P.; Kuran, P.; Kormunda, M.; Stengl, V.; Grygar, T.M.; Dosek, M.; Stastny, M.; Ederer, J.; Pilarova, V.; Vrtoch, L. Cerium dioxide as a new reactive sorbent for fast degradation of parathion methyl and some other organophosphates. *J. Rare Earths* **2014**, *32*, 360–370. [CrossRef]
19. Baker, P.A. Development of Peptide Nanotube-Modified Biosensors for Gas-Phase Organophosphate Detection. Master's Thesis, Graduate School of Engineering and Management, Air Force Institute of Technology, New York, NY, USA, 2013.
20. Musameh, M.; Notivoli, M.R.; Hickey, M.; Huynh, C.P.; Hawkins, S.C.; Yousef, J.M.; Kyratzis, I.L. Carbon nanotube-Web modified electrodes for ultrasensitive detection of organophosphate pesticides. *Electrochim. Acta* **2013**, *101*, 209–215. [CrossRef]
21. Yang, Y.; Tu, H.; Zhang, A.; Du, D.; Lin, Y. Preparation and characterization of Au–ZrO_2–SiO_2 nanocomposite spheres and their application in enrichment and detection of organophosphorus agents. *J. Mater. Chem.* **2012**, *22*, 4977–4981. [CrossRef]
22. Van Dyk, J.S.; Pletschke, B. Review on the use of enzymes for the detection of organochlorine, organophosphate and carbamate pesticides in the environment. *Chemosphere* **2011**, *82*, 291–307. [CrossRef] [PubMed]
23. Sun, J.; Guo, L.; Bao, Y.; Xie, J. A simple, label-free AuNPs-based colorimetric ultrasensitive detection of nerve agents and highly toxic organophosphate pesticide. *Biosens. Bioelectron.* **2011**, *28*, 152–157. [CrossRef] [PubMed]
24. Urek, Š.K.; Lobnik, A. Fluorescent-based chemical sensor for organophosphate detection. In Proceedings of the SPIE Optics + Optoelectronics, Prague, Czech Republic, 18–21 April 2011; p. 80730Y.
25. Denet, E.; Espina-Benitez, M.B.; Pitault, I.; Pollet, T.; Blaha, D.; Bolzinger, M.-A.; Rodriguez-Nava, V.; Briancon, S. Metal oxide nanoparticles for the decontamination of toxic chemical and biological compounds. *Int. J. Pharm.* **2020**, *583*, 119373. [CrossRef] [PubMed]
26. Kim, K.; Tsay, O.G.; Atwood, D.A.; Churchill, D.G. Destruction and detection of chemical warfare agents. *Chem. Rev.* **2011**, *111*, 5345–5403. [CrossRef]
27. Gordon, W.O.; Morris, J.R.; Tissue, B.M. Control of morphology in inert-gas condensation of metal oxide nanoparticles. *J. Mater. Sci.* **2009**, *44*, 4286–4295. [CrossRef]
28. Eilers, H.; Tissue, B.M. Synthesis of nanophase ZnO, Eu_2O_3, and ZrO_2 by gas-phase condensation with cw-CO_2 laser heating. *Mater. Lett.* **1995**, *24*, 261–265. [CrossRef]
29. Suryanarayanan, V.; Tom, R.T.; Nair, A.S.; Pradeep, T. Electrochemical investigations of oxide coated nanoparticles. *Proc. Natl. Acad. Sci. USA* **2004**, *70*, 483–488.
30. Mitchell, M.B.; Sheinker, V.N.; Mintz, E.A. Adsorption and decomposition of dimethyl methylphosphonate on metal oxides. *J. Phys. Chem. B* **1997**, *101*, 11192–11203. [CrossRef]
31. Soliz, J.R.; Klevitch, A.D.; Harris, C.R.; Rossin, J.A.; Ng, A.; Stroud, R.M.; Hauser, A.J.; Peterson, G.W. Structural Impact on Dielectric Properties of Zirconia. *J. Phys. Chem. C* **2016**, *120*, 26834–26840. [CrossRef]
32. DeSario, P.A.; Gordon, W.O.; Balboa, A.; Pennington, A.M.; Pitman, C.L.; McEntee, M.; Pietron, J.J. Photoenhanced degradation of sarin at Cu/TiO_2 composite aerogels: Roles of bandgap excitation and surface plasmon excitation. *ACS Appl. Mater. Interfaces* **2021**, *13*, 12550–12561. [CrossRef]
33. Štengl, V.C.; St'astný, M.; Janoš, P.; Mazanec, K.; Perez-Diaz, J.L.; Štenglová-Netíková, I.R. From the decomposition of chemical warfare agents to the decontamination of cytostatics. *Ind. Eng. Chem. Res.* **2018**, *57*, 2114–2122. [CrossRef]
34. Wu, R.-A.; Lin, C.W.; Tseng, W.J. Preparation of electrospun Cu-doped α-Fe_2O_3 semiconductor nanofibers for NO_2 gas sensor. *Ceram. Int.* **2017**, *43*, S535–S540. [CrossRef]
35. Harraz, F.A.; Faisal, M.; Jalalah, M.; Almadiy, A.; Al-Sayari, S.; Al-Assiri, M. Conducting polythiophene/α-Fe_2O_3 nanocomposite for efficient methanol electrochemical sensor. *Appl. Surf. Sci.* **2020**, *508*, 145226. [CrossRef]
36. Guo, L.; Kou, X.; Ding, M.; Wang, C.; Dong, L.; Zhang, H.; Feng, C.; Sun, Y.; Gao, Y.; Sun, P. Reduced graphene oxide/α-Fe_2O_3 composite nanofibers for application in gas sensors. *Sens. Actuators B Chem.* **2017**, *244*, 233–242. [CrossRef]
37. Geupel, A.; Schönauer, D.; Röder-Roith, U.; Kubinski, D.; Mulla, S.; Ballinger, T.; Chen, H.-Y.; Visser, J.; Moos, R. Integrating nitrogen oxide sensor: A novel concept for measuring low concentrations in the exhaust gas. *Sens. Actuators B Chem.* **2010**, *145*, 756–761. [CrossRef]
38. Boarino, L.; Baratto, C.; Geobaldo, F.; Amato, G.; Comini, E.; Rossi, A.; Faglia, G.; Lerondel, G.; Sberveglieri, G. NO_2 monitoring at room temperature by a porous silicon gas sensor. *Mater. Sci. Eng. B* **2000**, *69*, 210–214. [CrossRef]
39. Chen, D.A.; Ratliff, J.S.; Hu, X.; Gordon, W.O.; Senanayake, S.D.; Mullins, D.R. Dimethyl methylphosphonate decomposition on fully oxidized and partially reduced ceria thin films. *Surf. Sci.* **2010**, *604*, 574–587. [CrossRef]
40. Janoš, P.; Henych, J.; Pelant, O.; Pilařová, V.; Vrtoch, L.; Kormunda, M.; Mazanec, K.; Štengl, V. Cerium oxide for the destruction of chemical warfare agents: A comparison of synthetic routes. *J. Hazard. Mater.* **2016**, *304*, 259–268. [CrossRef]
41. Khuspe, G.; Sakhare, R.; Navale, S.; Chougule, M.; Kolekar, Y.; Mulik, R.; Pawar, R.; Lee, C.; Patil, V. Nanostructured SnO_2 thin films for NO_2 gas sensing applications. *Ceram. Int.* **2013**, *39*, 8673–8679. [CrossRef]
42. Sakhare, R.; Khuspe, G.; Navale, S.; Mulik, R.; Chougule, M.; Pawar, R.; Lee, C.; Sen, S.; Patil, V. Nanocrystalline SnO_2 thin films: Structural, morphological, electrical transport and optical studies. *J. Alloys Compd.* **2013**, *563*, 300–306. [CrossRef]
43. Mohanta, D.; Gupta, S.V.; Gadore, V.; Paul, S.; Ahmaruzzaman, M. SnO_2 nanoparticles–CeO_2 nanorods enriched with oxygen vacancies for bifunctional sensing performances toward toxic CO gas and arsenate ions. *ACS Omega* **2022**, *7*, 20357–20368. [CrossRef] [PubMed]

44. Navale, S.T.; Bandgar, D.K.; Nalage, S.R.; Khuspe, G.D.; Chougule, M.A.; Kolekar, Y.D.; Sen, S.; Patil, V.B. Synthesis of Fe_2O_3 nanoparticles for nitrogen dioxide gas sensing applications. *Ceram. Int.* **2013**, *39*, 6453–6460. [CrossRef]
45. Pan, H.; Li, Z.; Lou, C.; Lei, G.; Xie, J.; Zheng, W.; Liu, X.; Zhang, J. Anchoring Fe_2O_3 nanosheets on NiO nanoprisms to regulate the electronic properties for improved n-butanol detection. *Sens. Actuators B Chem.* **2022**, *354*, 131223. [CrossRef]
46. Wang, Y.; Wang, Y.-J.; Chen, S.-S.; Liu, C.-C.; Chen, L.; Liu, Z.-G.; Guo, Z. Chemiresistive sensor based on hollow Fe_2O_3 octahedrons incorporated into porous In_2O_3 nanofibers for enhanced sensing performance and recognition toward triethylamine. *Sens. Actuators B Chem.* **2023**, *393*, 134129. [CrossRef]
47. Baratto, C.; Sberveglieri, G.; Onischuk, A.; Caruso, B.; Di Stasio, S. Low temperature selective NO_2 sensors by nanostructured fibres of ZnO. *Sens. Actuators B Chem.* **2004**, *100*, 261–265. [CrossRef]
48. Mun, Y.; Park, S.; An, S.; Lee, C.; Kim, H.W. NO_2 gas sensing properties of Au-functionalized porous ZnO nanosheets enhanced by UV irradiation. *Ceram. Int.* **2013**, *39*, 8615–8622. [CrossRef]
49. Cheng, Y.; Guo, H.; Wang, Y.; Zhao, Y.; Li, Y.; Liu, L.; Li, H.; Duan, H. Low cost fabrication of highly sensitive ethanol sensor based on Pd-doped α-Fe_2O_3 porous nanotubes. *Mater. Res. Bull.* **2018**, *105*, 21–27. [CrossRef]
50. Radhakrishnan, S.; Krishnamoorthy, K.; Sekar, C.; Wilson, J.; Kim, S.J. A highly sensitive electrochemical sensor for nitrite detection based on Fe_2O_3 nanoparticles decorated reduced graphene oxide nanosheets. *Appl. Catal. B Environ.* **2014**, *148*, 22–28. [CrossRef]
51. Yin, Y.; Zhang, X.; Sun, C. Transition-metal-doped Fe_2O_3 nanoparticles for oxygen evolution reaction. *Prog. Nat. Sci. Mater. Int.* **2018**, *28*, 430–436. [CrossRef]
52. Friedrich, R.P.; Cicha, I.; Alexiou, C. Iron oxide nanoparticles in regenerative medicine and tissue engineering. *Nanomaterials* **2021**, *11*, 2337. [CrossRef]
53. Dadfar, S.M.; Roemhild, K.; Drude, N.I.; von Stillfried, S.; Knüchel, R.; Kiessling, F.; Lammers, T. Iron oxide nanoparticles: Diagnostic, therapeutic and theranostic applications. *Adv. Drug Deliv. Rev.* **2019**, *138*, 302–325. [CrossRef] [PubMed]
54. Niska, K.; Zielinska, E.; Radomski, M.W.; Inkielewicz-Stepniak, I. Metal nanoparticles in dermatology and cosmetology: Interactions with human skin cells. *Chem. Biol. Interact.* **2018**, *295*, 38–51. [CrossRef] [PubMed]
55. Harris, C.R.; Soliz, J.R.; Klevitch, A.D.; Bartz, M.J.; Rossin, J.A.; Fountain, A.W.; Hauser, A.J.; Peterson, G.W. Sensing of NO_2 with zirconium hydroxide via frequency-dependent electrical impedance spectroscopy. *Dalton Trans.* **2017**, *46*, 10791–10797. [CrossRef] [PubMed]
56. Peterson, G.W.; Mcentee, M.; Harris, C.R.; Klevitch, A.D.; Fountain, A.W.; Soliz, J.; Balboa, A.; Hauser, A. Detection of an explosive simulant via electrical impedance spectroscopy utilizing the UiO-66-NH_2 metal–organic framework. *Dalton Trans.* **2016**, *45*, 17113–17116. [CrossRef]
57. Henderson, M.A. Surface Chemistry of Trimethyl Phosphate on α-Fe_2O_3. *J. Phys. Chem. C* **2011**, *115*, 23527–23534. [CrossRef]
58. Henderson, M.A.; Jin, T.; White, J.M. A TPD/AES study of the interaction of dimethyl methylphosphonate with iron oxide (.alpha.-Fe_2O_3) and silicon dioxide. *J. Phys. Chem.* **1986**, *90*, 4607–4611. [CrossRef]
59. Tesfai, T.M.; Sheinker, V.N.; Mitchell, M.B. Decomposition of Dimethyl Methylphosphonate (DMMP) on Alumina-Supported Iron Oxide. *J. Phys. Chem. B* **1998**, *102*, 7299–7302. [CrossRef]
60. Zhang, X.; Niu, Y.; Meng, X.; Li, Y.; Zhao, J. Structural evolution and characteristics of the phase transformations between α-Fe_2O_3, Fe_3O_4 and γ-Fe_2O_3 nanoparticles under reducing and oxidizing atmospheres. *CrystEngComm* **2013**, *15*, 8166–8172. [CrossRef]
61. Chen, L.X.; Liu, T.; Thurnauer, M.C.; Csencsits, R.; Rajh, T. Fe_2O_3 nanoparticle structures investigated by X-ray absorption near-edge structure, surface modifications, and model calculations. *J. Phys. Chem. B* **2002**, *106*, 8539–8546. [CrossRef]
62. Nagao, M.; Otani, M.; Tomita, H.; Kanzaki, S.; Yamada, A.; Kanno, R. New three-dimensional electrode structure for the lithium battery: Nano-sized γ-Fe_2O_3 in a mesoporous carbon matrix. *J. Power Sources* **2011**, *196*, 4741–4746. [CrossRef]
63. Teramura, Y.; Tanaka, A.; Jo, T. Effect of coulomb interaction on the X-ray magnetic circular dichroism spin sum rule in 3 d transition elements. *J. Phys. Soc. Jpn.* **1996**, *65*, 1053–1055. [CrossRef]
64. Nibarger, J.; Lopusnik, R.; Celinski, Z.; Silva, T. Variation of magnetization and the Landé g factor with thickness in Ni–Fe films. *Appl. Phys. Lett.* **2003**, *83*, 93–95. [CrossRef]
65. Wu, Z.Y.; Gota, S.; Jollet, F.; Pollak, M.; Gautier-Soyer, M.; Natoli, C.R. Characterization of iron oxides by x-ray absorption at the oxygen K edgeusing a full multiple-scattering approach. *Phys. Rev. B* **1997**, *55*, 2570–2577. [CrossRef]
66. Colliex, C.; Manoubi, T.; Ortiz, C. Electron-energy-loss-spectroscopy near-edge fine structures in the iron-oxygen system. *Phys. Rev. B* **1991**, *44*, 11402. [CrossRef]
67. Mohamed, A.Y.; Park, W.G.; Cho, D.-Y. Chemical structure and magnetism of FeOx/Fe_2O_3 interface studied by X-ray absorption spectroscopy. *Magnetochemistry* **2020**, *6*, 33. [CrossRef]
68. Bielecki, M.; Witkiewicz, Z.; Rogala, P. Sensors to detect sarin simulant. *Crit. Rev. Anal. Chem.* **2021**, *51*, 299–311. [CrossRef]
69. Kalnina, R.; Priednieks, V.; Lukins, K.; Gasparjans, A.; Rijkure, A. Corrosion and electrochemical impedance spectroscopy of thin TiALN and TiCN PVD coatings for protection of ballast water screen filters. *Latv. J. Phys. Tech. Sci.* **2021**, *58*, 64–78. [CrossRef]
70. Li, X.; Dutta, P.K. Interaction of Dimethylmethylphosphonate with Zeolite Y: Impedance-Based Sensor for Detecting Nerve Agent Simulants. *J. Phys. Chem. C* **2010**, *114*, 7986–7994. [CrossRef]
71. Sohrabi, H.; Ghasemzadeh, S.; Ghoreishi, Z.; Majidi, M.R.; Yoon, Y.; Dizge, N.; Khataee, A. Metal-organic frameworks (MOF)-based sensors for detection of toxic gases: A review of current status and future prospects. *Mater. Chem. Phys.* **2023**, *299*, 127512. [CrossRef]

72. Chittibabu, S.K.; Chintagumpala, K.; Chandrasekhar, A. Porous dielectric materials based wearable capacitance pressure sensors for vital signs monitoring: A review. *Mater. Sci. Semicond. Process.* **2022**, *151*, 106976. [CrossRef]
73. Liu, S.; Duan, R.; He, S.; Liu, H.; Huang, M.; Liu, X.; Liu, W.; Zhu, C. Research progress on dielectric properties of PU and its application on capacitive sensors and OTFTs. *React. Funct. Polym.* **2022**, *181*, 105420. [CrossRef]
74. Afroozeh, A.; Zeinali, B. Improving the sensitivity of new passive optical fiber ring sensor based on meta-dielectric materials. *Opt. Fiber Technol.* **2022**, *68*, 102797. [CrossRef]
75. Liu, K.; Qin, M.; Shi, Q.; Wang, G.; Zhang, J.; Ding, N.; Xi, H.; Liu, T.; Kong, J.; Fang, Y. Fast and selective detection of trace chemical warfare agents enabled by an ESIPT-based fluorescent film sensor. *Anal. Chem.* **2022**, *94*, 11151–11158. [CrossRef] [PubMed]
76. Revilla-Cuesta, A.; Abajo-Cuadrado, I.; Medrano, M.; Salgado, M.M.; Avella, M.; Rodríguez, M.T.; García-Calvo, J.; Torroba, T. Silica Nanoparticle/Fluorescent Dye Assembly Capable of Ultrasensitively Detecting Airborne Triacetone Triperoxide: Proof-of-Concept Detection of Improvised Explosive Devices in the Workroom. *ACS Appl. Mater. Interfaces* **2023**, *15*, 32024–32036. [CrossRef]
77. Korotcenkov, G.; Brinzari, V.; Cho, B.K. Conductometric gas sensors based on metal oxides modified with gold nanoparticles: A review. *Microchim. Acta* **2016**, *183*, 1033–1054. [CrossRef]
78. Amoah, P.K.; Hassan, Z.M.; Lin, P.; Redel, E.; Baumgart, H.; Obeng, Y.S. Broadband dielectric spectroscopic detection of ethanol: A side-by-side comparison of ZnO and HKUST-1 MOFs as sensing media. *Chemosensors* **2022**, *10*, 241. [CrossRef]
79. Koo, W.-T.; Jang, J.-S.; Kim, I.-D. Metal-organic frameworks for chemiresistive sensors. *Chem* **2019**, *5*, 1938–1963. [CrossRef]
80. Sharma, A.K.; Mahajan, A. Potential applications of chemiresistive gas sensors. In *Carbon Nanomaterials and Their Nanocomposite-Based Chemiresistive Gas Sensors*; Elsevier: Amsterdam, The Netherlands, 2023; pp. 223–245.
81. Patil, L.A.; Bari, A.R.; Shinde, M.D.; Deo, V.; Kaushik, M.P. Detection of dimethyl methyl phosphonate—A simulant of sarin: The highly toxic chemical warfare—Using platinum activated nanocrystalline ZnO thick films. *Sens. Actuators B Chem.* **2012**, *161*, 372–380. [CrossRef]
82. Powroźnik, P.; Solecka, B.; Pander, P.; Jakubik, W.; Dias, F.B.; Krzywiecki, M. Zinc Phthalocyanine Sensing Mechanism Quantification for Potential Application in Chemical Warfare Agent Detectors. *Sensors* **2022**, *22*, 9947. [CrossRef]